

# Susceptibility Phase Imaging With Improved Image Contrast Using Moving Window Phase Gradient Fitting and Minimal Filtering

Andrew J. Walsh, BSc,<sup>1</sup> Amir Eissa, PhD,<sup>1</sup> Gregg Blevins, MD,<sup>2</sup> and Alan H. Wilman, PhD<sup>1\*</sup>

**Purpose:** To enhance image contrast in susceptibility phase imaging using a new method of background phase removal.

**Materials and Methods:** A background phase removal method is proposed that uses the spatial gradient of the raw phase image to perform a moving window third-order local polynomial estimation and correction of the raw phase image followed by minimal high pass filtering. The method is demonstrated in simulation, 10 healthy volunteers, and 5 multiple sclerosis patients in comparison to a standard phase filtering approach.

**Results:** Compared to standard phase filtering, the new method increased phase contrast with local background tissue in subcortical gray matter, cortical gray matter, and multiple sclerosis lesions by  $67\% \pm 33\%$ ,  $13\% \pm 7\%$ , and  $48\% \pm 19\%$ , respectively (95% confidence interval). In addition, the new method removed more phase wraps in areas of rapidly changing background phase.

**Conclusion:** Local phase gradient fitting combined with minimal high pass filtering provides better tissue depiction and more accurate phase quantification than standard filtering.

**Key Words:** phase; susceptibility-weighted; spatial gradient; unwrapping; filtering

**J. Magn. Reson. Imaging 2012;36:1460–1469.**

© 2012 Wiley Periodicals, Inc.

THE PRIMARY SOURCES of susceptibility affecting phase contrast in brain tissue are iron, myelin, calcium, and air (1,2). Visualization or quantification of

these susceptibility sources can be achieved with phase imaging (3), susceptibility-weighted imaging (SWI) (4), or susceptibility mapping (5). However, all of these methods first require background phase removal. Background phase arises from sources of magnetic field variation external to the region of interest (ROI). This includes boundaries between regions of significantly different magnetic susceptibility, most notably at the air–tissue interfaces in the sinuses and at the surface of the head (6).

The most widely reported phase removal method uses a threshold  $k$ -space, high pass filter approach to remove slowly varying background phase due to susceptibility sources external to the brain tissue (4,7–9). Limitations of the standard filtering method include suppression of phase values in larger structures and lack of background removal in areas of the brain with rapidly varying background phase, such as near the paranasal sinuses (10). In addition, phase quantification in deep gray matter is altered by strong filter values while weaker filters might not properly remove background phase (11). Variable filters have been proposed for improved visualization (12–14), but may have potentially confounding diagnostic value due to nonuniform processing. As well, assumptions are made about edge locations in the brain which could be problematic when visualizing certain localized pathologies near the brain surface such as cortical multiple sclerosis (MS) lesions or cortical vein thrombosis (15). Using the weakest possible filter while still removing all of the global background phase is desirable for maximum contrast; however, these goals are contradictory.

Recent alternatives to filtering include sophisticated harmonic artifact reduction for phase data (SHARP) (16) and projection onto dipole fields (PDF) (17). As well, polynomial fitting to the whole brain (18) or within a moving window (19) have also been implemented. However, these methods experience problems near the outer brain surface with removal of pixels using SHARP or violation of assumptions using PDF. Moreover, the polynomial fitting methods can also suffer from phase suppression in larger structures if the polynomial matches the structure contour, rather than the background phase, because of a high-order polynomial or small fitting territory. All of these

<sup>1</sup>Department of Biomedical Engineering, Faculty of Medicine and Dentistry, University of Alberta, Edmonton, Alberta, Canada.

<sup>2</sup>Division of Neurology, Faculty of Medicine and Dentistry, University of Alberta, Edmonton, Alberta, Canada.

Contract grant sponsor: Natural Sciences and Engineering Research Council of Canada (NSERC); Contract grant sponsor: Canadian Institutes of Health Research (CIHR); Contract grant sponsor: Multiple Sclerosis Society of Canada; Contract grant sponsor: Vanier Canada Graduate Scholarship and an Alberta Innovates Health Solutions MD/PhD studentship (to A.J.W.).

\*Address reprint requests to: A.H.W., 1098 RTF, Department of Biomedical Engineering, University of Alberta Edmonton, Alberta, Canada T6G 2V2. E-mail: alan.wilman@ualberta.ca

Received September 6, 2011; Accepted June 28, 2012.

DOI 10.1002/jmri.23768

View this article online at [wileyonlinelibrary.com](http://wileyonlinelibrary.com).

alternative methods require phase unwrapping prior to background phase removal. There is a wide variety of unwrapping algorithms that are generally effective, but many algorithms can be less robust in areas of extremely large phase variation or areas with a low signal-to-noise ratio (SNR) as described by Bagher-Ebadian et al (20), Rauscher et al (21), Langley and Zhao (22), and Witoszynkyj et al (23). For phase unwrapping, the  $\pm\pi$  surfaces are trivial to detect provided they are distinct from regions where adjacent pixels differ by less than  $\pi$ , and there is adequate SNR. In cases of excessive noise, rapidly varying phase or phase discontinuities, phase unwrapping becomes very difficult, although complex algorithms may overcome this (21,22).

In this work, we apply a background phase removal method that determines local polynomial coefficients to the raw phase image without requiring unwrapping or image masking. The method relies on a moving window analytical estimation of the raw phase based on a least-squares calculation of the spatial gradient of the raw phase image to locally smooth the background phase followed by the application of a weak filter. The new method is tested against standard phase filtering in simulation, healthy volunteers, and MS patients.

## MATERIALS AND METHODS

### Phase Removal Method Overview

The new phase removal method makes use of a moving window approach to perform local, analytical determination of polynomial coefficients of the raw phase using the phase gradient. There are five main steps: 1) computation of spatial gradient maps in the x and y direction from the raw phase; 2) analytical determination of local polynomial coefficients to the raw phase from the phase gradient maps within a square fitting window; 3) phase correction of the original complex image based on the determined polynomial coefficients producing a locally smoothed phase profile within the fitting window; 4) minimal high pass filtering using a  $k$ -space approach; then 5) extraction from each corrected image of a square portion, called the extraction window, that is centered within the square fitting window. Steps 2 to 5 are repeated, using the information from step 1, moving both the fitting and extraction window by half the dimension of the extraction window in the x and y direction until the full image is covered. The individual extraction windows are subsequently combined into a final image. The entire procedure is outlined in Fig. 1. Unwrapping is not required as the spatial gradient is used to locally estimate polynomial coefficients to the raw phase data using a least-squares approach to the gradient information where phase wraps, determined by extreme gradient values, are excluded from the fitting. If a polynomial were fit to the raw phase directly, rather than using the phase gradient, an unwrapping algorithm would be required.

### Phase Removal Method Details

In step 1, the spatial gradient of a 2D raw phase image is obtained in the x and y dimensions over the

whole image, creating two separate gradient maps. Both gradient maps, generated using the MatLab (MathWorks, Natick, MA) 2011a gradient function, are thresholded at  $\sqrt{g_x^2 + g_y^2} > 2.5$  rads/pixel, where  $g_x$  and  $g_y$  are the values of the gradient data in the x direction and y direction. The thresholded regions are excluded in the least-squares fit. The phase gradient at locations of phase wraps has a much higher gradient value than unaffected regions, which have gradient values of less than 1 rad/pixel in this work.

In step 2, the phase gradient data are used to locally estimate a third-order polynomial fit to the original phase data within each fitting window using a new gradient least-squares approach. The coefficients for a 2D polynomial estimate to the raw background phase are calculated by minimizing the residual of the partial derivatives of this polynomial to the gradient data. The analytical process is illustrated using a second-order polynomial fit, which can be extended to higher orders. Equations [1] to [6] show the sums of squares fit to the gradient data, where  $p(x,y)$  is the estimated polynomial fit to the original raw phase image,  $p_x$  is the estimated value of the gradient data in the x direction, and  $p_y$  is the estimated value of the gradient data in the y direction. The computed gradients of the original phase image are  $g_x$  and  $g_y$  in the x and y direction, respectively. A second-order polynomial fit with coefficients  $a_{0-5}$  is shown in Eq. [1], with Eqs. [2,3] illustrating the partial derivatives to  $p(x,y)$  in the x and y directions, respectively, Eq. [4] the minimization function, and Eqs. [5,6] the sum of squares fit.

$$p(x, y) = a_0 + a_1x + a_2y + a_3xy + a_4x^2 + a_5y^2 \quad [1]$$

$$p_x = \frac{\partial p}{\partial x} = a_1 + a_3y + a_42x \quad [2]$$

$$p_y = \frac{\partial p}{\partial y} = a_2 + a_3x + a_52y \quad [3]$$

$$Sr = \sum (g_x - a_1 - a_3y - a_42x)^2 + \sum (g_y - a_2 - a_3x - a_52y)^2 = \min \quad [4]$$

The index sum is over the pixels within the fitting window. Taking partial derivatives with respect to the constant terms gives:

$$\frac{\partial Sr}{\partial a_1} = -2 \sum (g_x - a_1 - a_3y - a_42x) = 0 \quad [5a]$$

$$\frac{\partial Sr}{\partial a_2} = -2 \sum (g_y - a_2 - a_3x - a_52y) = 0 \quad [5b]$$

$$\frac{\partial Sr}{\partial a_3} = -2 \sum (g_x - a_1 - a_3y - a_42x)y - 2 \sum (g_y - a_2 - a_3x - a_52y)x = 0 \quad [5c]$$

$$\frac{\partial Sr}{\partial a_4} = -2 \sum (g_x - a_1 - a_3y - a_42x)2x = 0 \quad [5d]$$

$$\frac{\partial Sr}{\partial a_5} = -2 \sum (g_y - a_2 - a_3x - a_52y)2y = 0 \quad [5e]$$

This can be rearranged to:

$$\begin{bmatrix} n & 0 & \sum y & 2\sum x & 0 \\ 0 & n & \sum x & 0 & 2\sum y \\ \sum y & \sum x & \sum x^2 + \sum y^2 & 2\sum xy & 2\sum xy \\ \sum x & 0 & \sum xy & 2\sum x^2 & 0 \\ 0 & \sum y & \sum xy & 0 & 2\sum y^2 \end{bmatrix} \begin{bmatrix} a_1 \\ a_2 \\ a_3 \\ a_4 \\ a_5 \end{bmatrix} \\
 = \begin{bmatrix} \sum g_x \\ \sum g_y \\ \sum g_x + \sum g_y \\ \sum g_x x \\ \sum g_y y \end{bmatrix} \quad [6]$$

where  $n$  is the number of data points used within the local fitting window and the index sum is over the pixels in this window.

In step 3 the whole original 2D complex image  $img_{orig}$  is multiplied, element by element, with a complex exponential to locally correct the phase within a fitting window. This exponential corrects the phase of the complex data with a local third order polynomial estimation of the background phase from coefficients determined in step 2. The whole original complex image is multiplied by this exponential function which yields the corrected image  $img_{corr}$ .

$$img_{corr}(x, y) = img_{orig}(x, y) \cdot e^{i(-p(x,y))} \quad [7]$$

where  $p(x,y)$  is from Eq. [1] and the constant  $a_0$  term is not included. This creates a smoothed phase profile within the fitting window and consequently the rest of the image may have a variable phase profile after this step.

In step 4, traditional  $k$ -space filtering is applied independently to each locally corrected image generated in step 3 with a less intense filter than standardly used. For traditional filtering, a 2D symmetrical Hanning window is constructed in the central portion of the image  $k$ -space and zero padded to the size of the full 2D image (24). The filter width is defined as the ratio of one dimension of the Hanning window divided by the total image size in that dimension. This central  $k$ -space window is Fourier transformed back to image space. The original 2D complex image is complex divided by the result, creating a high pass effect in phase. A typical filter reported is 0.125 filter width or greater when using a  $512 \times 512$  image matrix (25–27) for a similar echo time-to-field strength ratio used in this work. This corresponds to a central  $k$ -space representation of  $\pm 785$  rad/m for a 25.6 cm field of view (FOV). In the new method, a 0.0625 filter is also used which corresponds to  $\pm 393$  rad/m central  $k$ -space representation. Weak filtering is applied because higher terms in the polynomial fit are determined with the new fitting method, but not the constant term  $a_0$ . The weak filter moves the baseline of each region to zero, which reduces discontinuities between image segments. Other methods could normalize the baseline of individual extraction windows but filtering has the benefit of further removing slow varying background phase.

Finally, in step 5, after filtering each locally corrected image, the central region of the fitting window, the extraction window, is removed from each image

according to the location of the local fitting in step 2. This small window is multiplied by a spatial Hanning window of the same in-plane dimensions to further remove slight discontinuities at the window edges. All extraction windows are then combined into a final image where each individual extraction window has a one-quarter overlap with adjacent extraction windows. This overlap results in a final image with a flat profile, if each extraction window has the same offset and is initially flat.

### Simulation

A simulated 3D phase model was created in MatLab with dimensions  $512 \times 512 \times 512$ . Beginning with a large sphere of susceptibility  $-7$  ppm, a smaller sphere was removed from the edge. Several shapes were constructed inside this distribution including a cylinder with susceptibility of  $-4.82$  ppm, and ellipsoids and fine structures each with susceptibility of  $-4.70$  ppm. The Fourier transform of a dipole point source was multiplied to the Fourier transform of the entire susceptibility distribution and the result was inverse Fourier transformed to obtain the field projection from the susceptibility sources. Random phase noise from  $-\pi$  to  $+\pi$  was added outside of the distribution to simulate air. A similar model was created without the large spherical susceptibility distribution to obtain the ideal field representation of the internal structures for postfiltering comparison.

The simulation was tested with the standard filtering method and the new method, both with filter widths of 0.125 and 0.0625. Different square fitting (f) window sizes were tested with a constant square extraction (e) window of 16 pixels width and length. The side lengths of the fitting windows were 32, 48, and 64 pixels ( $32f \times 16e$ ,  $48f \times 16e$ ,  $64f \times 16e$ ). The images were visually compared for background field removal in areas with rapidly varying background phase and a profile was obtained from an internal structure to quantitatively evaluate the extent of phase alteration between methods and between different parameters using the new method.

### MRI Acquisition

Following institutional ethical approval and informed consent, images were obtained from 10 healthy volunteers and 5 patients with clinically definite relapsing-remitting MS using axial 2D gradient echo sequences with  $512 \times 256$  encoding matrix. Five volunteers were imaged at 3.0 T with a MR Research Systems console to examine the deep gray matter using seven 3-mm thick contiguous slices and 25 cm square FOV, TE/TR = 26/500 msec, and  $70^\circ$  flip angle. A 16-element cylindrical birdcage coil was used for transmission and reception. Five patients with relapsing remitting MS and five healthy volunteer were imaged using a 4.7 T Varian Unity Inova system with whole brain imaging using 50 2-mm thick contiguous slices,  $25.6 \times 19.25$  cm FOV, TE/TR = 15/1540 msec, and  $62^\circ$  flip angle. A 16-element cylindrical birdcage coil was used for transmission with a four-element

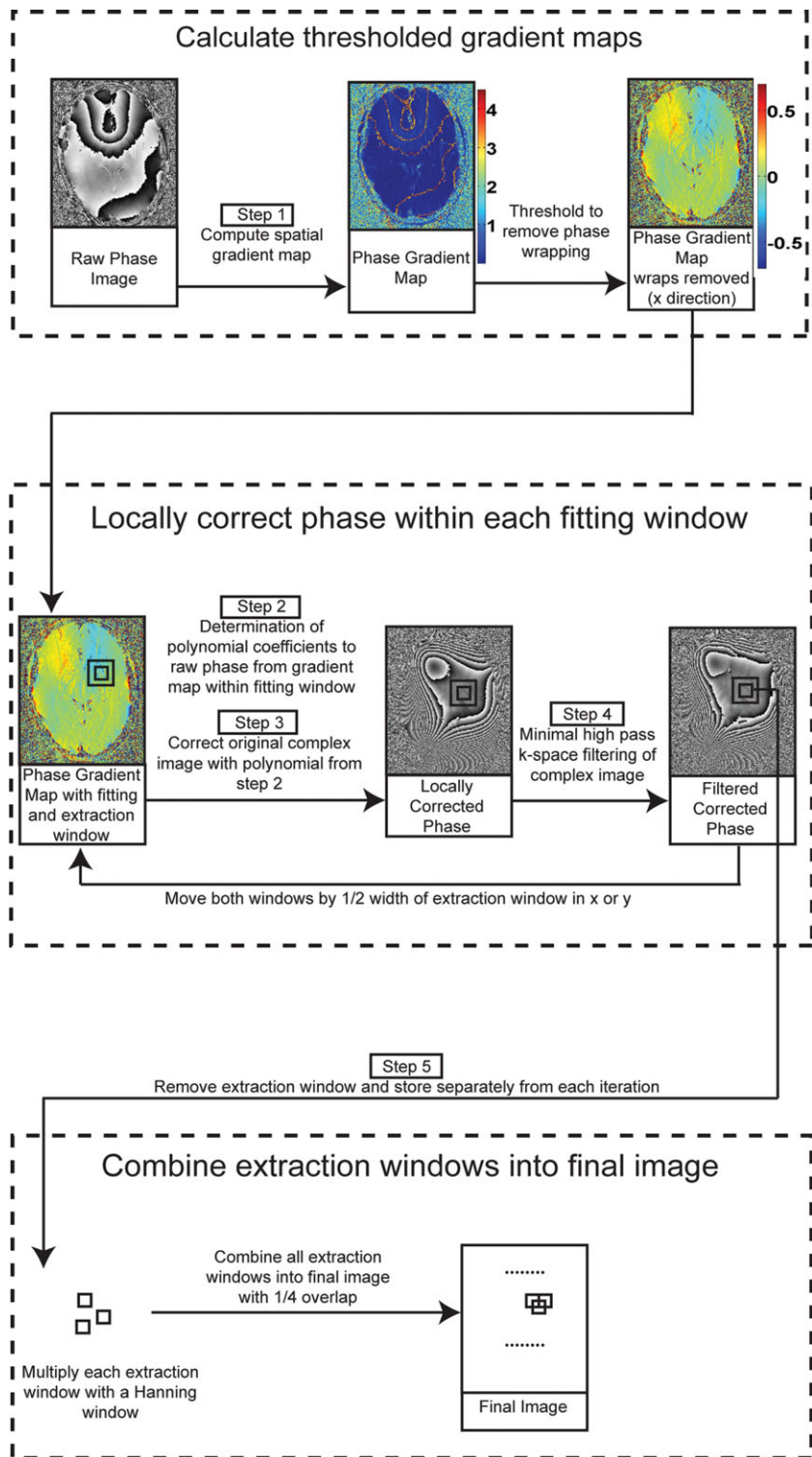


**Figure 1.** Flowchart illustrating the phase removal algorithm beginning with the raw phase image. Two square boxes show the square fitting (larger) and extraction (smaller) windows in steps 2–5. One iteration is shown; however, the moving fitting and extraction windows cover the full image for complete implementation. Color bars for the gradient maps are in units of radians/pixel. The phase gradient map directly after step 1 is calculated with  $\sqrt{g_x^2 + g_y^2}$  where  $g_x$  and  $g_y$  are the gradient maps following this show the x direction only; however, both x and y gradient maps are used in the algorithm.

circumscribing receiver array. The raw  $k$ -space data were zero-filled to  $512 \times 512$  pixels prior to phase removal processing using standard filtering and the new method with a range of fitting windows, extraction windows, and filter strengths. The 4.7 T acquisitions used an asymmetric FOV, thus giving different  $k$ -space step sizes in the two dimensions. For the 4.7T images, the same absolute  $k$ -space cutoff was used for the filter in both dimensions, with the filter width definition based on the larger FOV in the frequency encoding dimen-

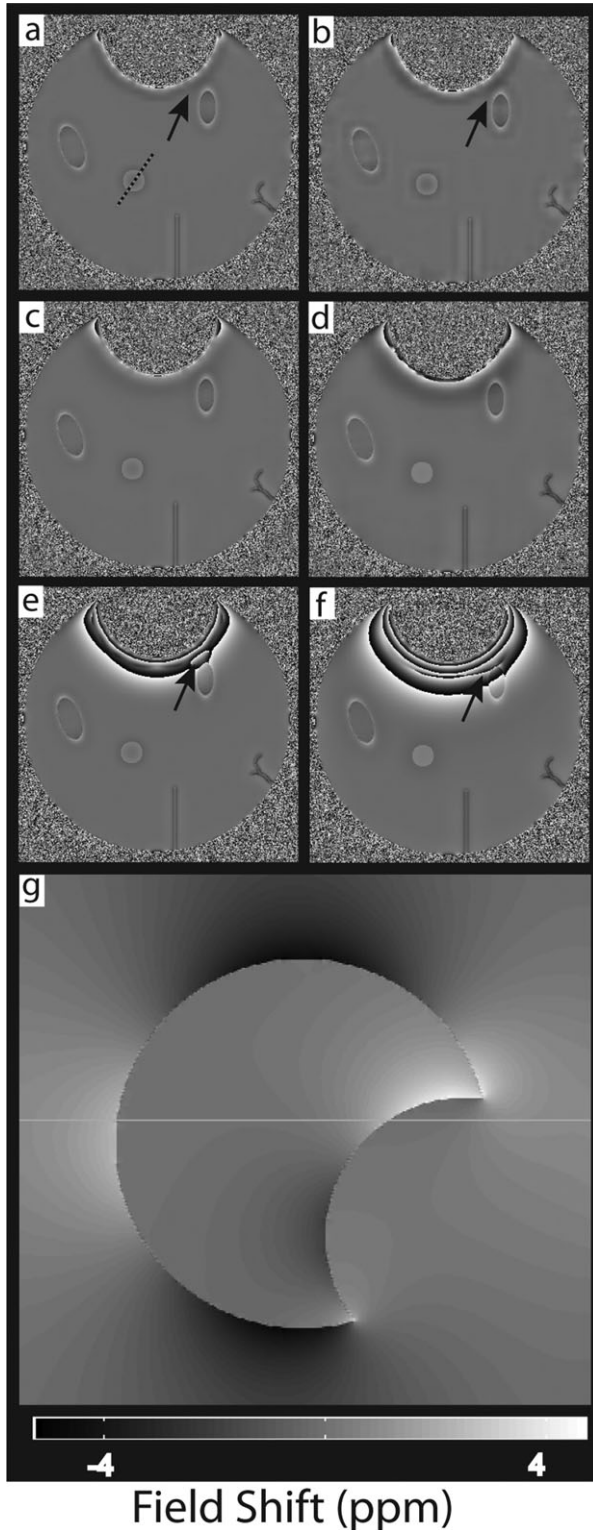
sion. With multiple element receiver arrays from the 4.7T MRI system, the full background phase removal algorithm was performed on each coil independently, then subsequently combined by weighting each phase channel by the magnitude image squared.

### Image Analysis

Phase and SWI images using the new method and standard phase filtering were evaluated using both

ROI measurements and examination of background phase removal. Quantitative ROI analysis was used to optimize parameters for deep gray matter contrast at 3.0 T. Phase measurements of the globus pallidus (GP), putamen (PUT), head of the caudate (CAUD), and cortical gray matter (GM) were referenced to nearby white matter (WM) that was <5 mm from each structure and compared between filtering methods using a paired *t*-test. As well, profiles were obtained

through the right globus pallidus and putamen, registered, and averaged across the five subjects, then compared between phase removal methods. The profiles were manually selected based on visual correspondence of location and angle in each subject. Registration was implemented using a custom MatLab function to align structures borders and correct any baseline discrepancies of the 1D profiles. At 4.7 T, 25 significant WM lesions in patients with MS were identified based on phase hypointensity and T2 hyperintensity. These lesions were compared to background phase measures in nearby tissue <5 mm away. The contrast between lesions using the new method and standard phase filtering was compared with a paired *t*-test. Qualitative analysis examined images from five healthy subjects at 4.7 T for phase wrap removal superior to the paranasal sinuses and auditory canals. Edge depiction and phase wrap removal were compared to the standard filtering method. In addition, a direct polynomial fit that used phase unwrapping was also compared for phase wrap removal. This method used the same moving window algorithm, but with step 1 replaced with unwrapping using PRELUDE in 2D mode (28) or PhiUn (23) and with step 2, the gradient fitting, replaced with a direct third-order polynomial fit to the unwrapped phase.



## RESULTS

### Simulation

Regions near strong background field variation are better visualized with the new method compared to standard filtering (Fig. 2). The ellipsoid, near the top of the images (arrow), is not affected by phase wrapping with the new method because it provides better elimination of background field shifts (Fig. 2a,b) compared to standard filtering (Fig. 2e,f). Since the gradient of the raw phase is rapidly changing near this edge of the large spherical susceptibility distribution, smaller fitting windows and higher filter strengths better eliminate background contributions in Fig. 2a compared to a half strength filter and larger fitting window in Fig. 2d. However, all of the different parameters tested with the new method eliminate more

**Figure 2.** Phase susceptibility simulation of a spherical susceptibility distribution with regions removed to create internal background field effects. Internal shapes include a cylinder with the axis along the inferior superior direction, two ellipsoids, and two finer structures. The new phase removal method is shown in axial images using two filtering widths 0.125 (a,c) and 0.0625 (b,d). In (a,b) the square fitting and extraction window is  $32f \times 16e$ , while (c,d) use a larger fitting window with same extraction window  $64f \times 16e$ . Comparison with the standard filtering method is made in (e,f) using the same filter strengths (e) 0.125 and (f) 0.0625 filter strength. **g:** Sagittal view of field shift from global susceptibility distribution with location of axial imaging plane of a-f shown. The simulated images use an inverted gray scale for profile comparison. Arrows show difference in background phase removal between methods.

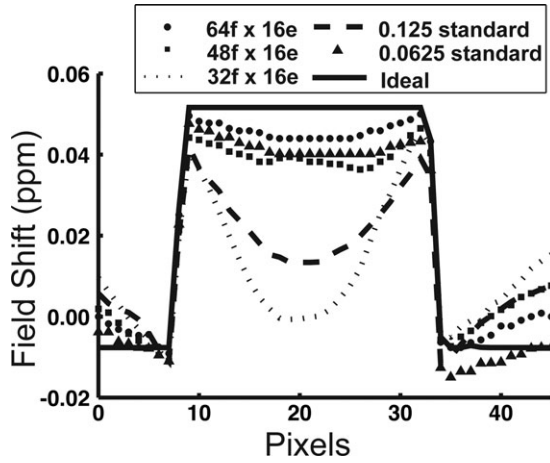


**Figure 3.** Profile through the large cylinder in Fig. 2 (dotted line) with the new filtering method using 0.0625 filter strength and three different square fitting (f) and extraction (e) windows. The ideal field shift from the cylinder is shown with no background phase removal and the absence of susceptibility effect from the large sphere. The standard methods are also compared using 0.125 and 0.0625 filter strength.

phase wrapping compared to the standard method (Fig. 2).

The fitting window size affects measured phase within large structures as illustrated in Fig. 2 and the profiles in Fig. 3. The fitting window must be at least as large as the structure of interest to avoid suppression of phase values in the center of the structure which is apparent for a fitting window of size 32 (Fig. 2b, 3). Finer structures have equivalent contrast using either the standard or new phase removal method, yet slight hyperintensities are present in the simulation with a small fitting window of size 32. Using a standard filter with a low strength of 0.0625 does not remove the background phase properly, while the new method, with the same filter strength, matches the ideal field shift more accurately (Fig. 3).

**In Vivo**

From the phase measures at 3.0 T, the optimum fitting window size is 64 for a 512 × 512 image matrix at TE = 26 msec while different extraction window sizes produce equivalent results (Fig. 4). Quantitative phase measures at 3.0 T with the new method using optimized parameters reveal markedly different results from the standard method (Table 1). The contrast is increased in the putamen by 31 ± 42%, globus pallidus by 26 ± 13%, caudate by 329 ± 147%, and cortical gray/white matter by 13 ± 7% (95% confidence interval [CI]). The increase in contrast between methods is significant ( $P < 0.05$ ) for all measured structures except the putamen.

Figure 5 shows 3.0 T images from a healthy volunteer where, in larger brain structures, the phase is less affected by filtering using the new method (Fig. 5a,b). Standard filtering with a weak filter of 0.0625 (Fig. 5c) does not properly remove the background phase and

wraps are visible in structures of interest. Figure 5e shows the average phase contrast from five individuals through a profile of the putamen and globus pallidus. With the new method, the phase is much less suppressed in the globus pallidus (Fig. 5e), while the phase in the putamen is similar. Using larger fitting windows slightly decreases the phase contrast in the middle of large structures with flat profiles, such as the globus pallidus. Similar to simulated images, phase suppression in large structures is also seen in vivo when the fitting window size is less than 32.

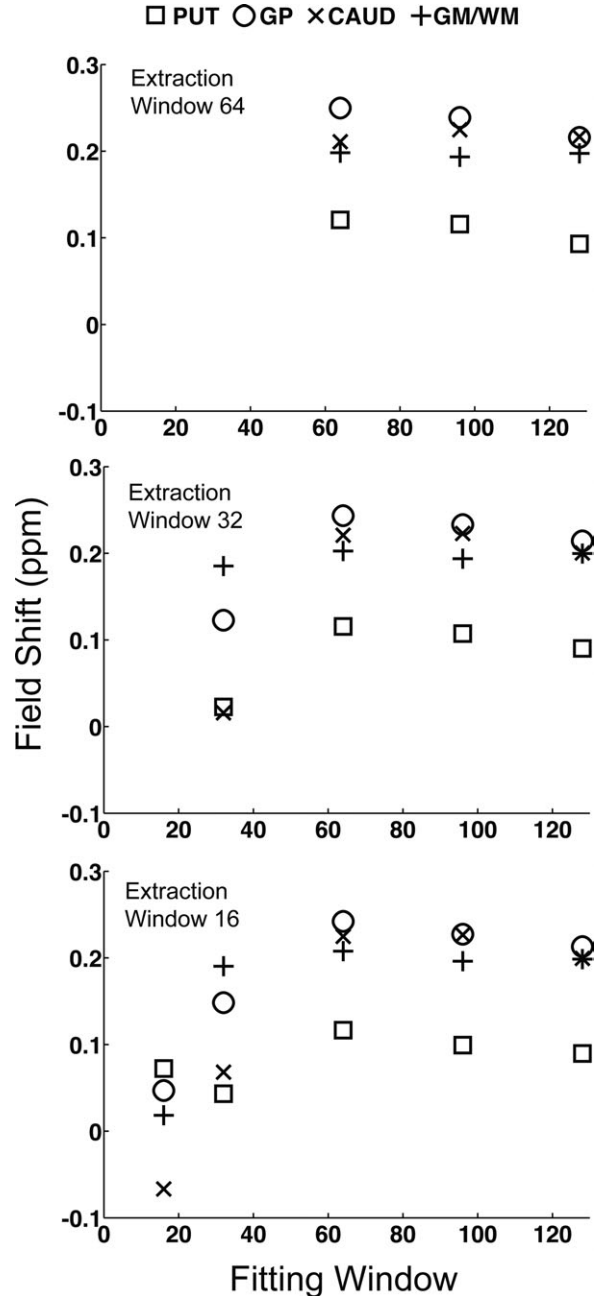


**Figure 4.** Contrast between deep gray matter structures or cortical gray matter and area of adjacent white matter at 3.0 T using different fitting window sizes and extraction window sizes. The filter strength is 0.0625. 3.0 T images use an inverted gray scale.

Table 1  
Phase Contrast Relative to Local White Matter Between New and Standard Phase Removal Methods Using Five Subjects at 3.0 T<sup>a</sup>

Structure	New method filter strength 0.0625		P-value <sup>b</sup>
	fitting = 64 extraction = 32 avg ± SD	Standard method filter strength 0.125 avg ± SD	
PUT	0.116 ± 0.044	0.088 ± 0.039	0.13
GP	0.243 ± 0.049	0.192 ± 0.054	0.001
CAUD	0.221 ± 0.166	0.067 ± 0.088	0.006
GM/WM	0.203 ± 0.071	0.180 ± 0.067	0.002

<sup>a</sup>Images from 3.0 T use an inverted gray scale.

<sup>b</sup>Analyzed with a repeated measures *t*-test.

Lesions in MS patients have greater contrast compared to adjacent tissue using the new phase removal method compared to the standard method. The contrast using the new method and standard filtering are  $-7.8 \pm 2.7$  ppb and  $-5.2 \pm 2.2$  ppb ( $P < 0.00001$ ), respectively, yielding a  $48\% \pm 19\%$  (95% CI) higher contrast with the new filtering method. Figure 6 illustrates lesion contrast between methods. Even in brain regions superior to the lateral ventricles, where background field contributions should be less than in more inferior brain regions, standard filtering with 0.0625 filter strength (Fig. 6c) does not remove the background phase and lesions are poorly visualized.

Compared to standard phase filtering, in all five healthy subjects at 4.7 T at TE = 15 msec, there are fewer phase wraps visualized using the new method with a filter strength of 0.0625 and square fitting and extraction windows of size 64 and 32, respectively. This is especially evident in areas near large susceptibility differences such as near the paranasal sinuses (Fig. 7). In one healthy subject shown in Fig. 7 the standard filtering method does not properly depict the substantia nigra and anterior vasculature. Even with low signal on the magnitude image near the auditory canals and paranasal sinuses, the phase image from the new method can reveal underlying tissues, while the standard method cannot because of phase wrapping. The background phase is more completely removed using a smaller fitting window with either filter strength of 0.125 or 0.0625 or a larger fitting window with higher filter strength of 0.125.

Direct polynomial fitting using unwrapped phase images are compared to the gradient fit method using the same five subjects at 4.7 T. In all five subjects, greater phase wrap removal is apparent using the gradient fitting compared to PRELUDE unwrapping. PRELUDE fails in some regions of low SNR and rapidly varying background phase, most notably directly superior to the auditory canals and paranasal sinuses. The new method with gradient fitting removes slightly more phase wraps than an advanced unwrapping algorithm, PhiUn, but the results are similar. The new background phase removal algorithm with gradient fitting or phase unwrapping with PRELUDE and PhiUn is shown in one of the healthy five subjects imaged at 4.7 T (Fig. 8).

## DISCUSSION

The two main advantages of the new background phase removal method over traditional phase filtering are improved visualization in areas affected by rapidly changing background fields and less phase suppression in deep gray matter structures for more accurate quantitative phase analysis and higher contrast.

The new method has few assumptions in its implementation. Phase unwrapping is not required prior to

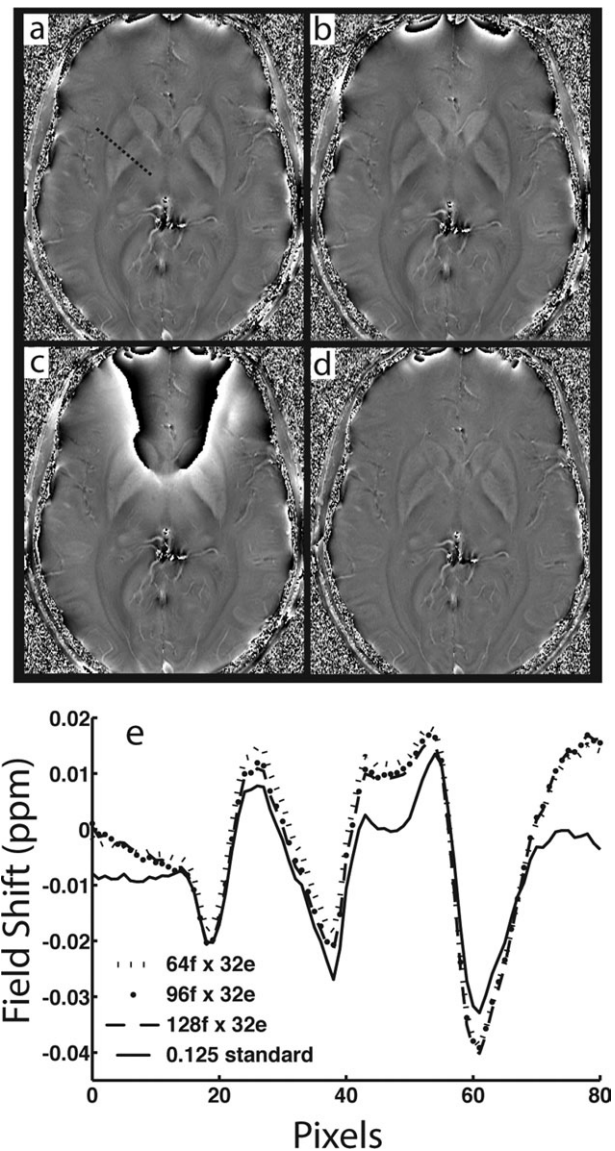


**Figure 5.** Axial image of deep gray matter structures at 3.0 T using the new gradient filtering method with 0.0625 filter strength and (a)  $64f \times 32e$  and (b)  $128f \times 32e$  square fitting and extraction window, respectively. Standard filtering with (c) 0.0625 filter strength and (d) 0.125 filter strength. **e:** Average profile through the center of the PUT and GP (dotted line in a) of five subjects using standard filter with 0.125 and new filtering methods with  $64f \times 32e$ ,  $96f \times 32e$  and  $128f \times 32e$  square fitting and extraction windows, respectively. The profile through the PUT and GP with standard filtering using 0.0625 filter strength is not shown in (e) because of visible phase wrapping. The images from 3.0 T use an inverted gray scale for profile comparison.

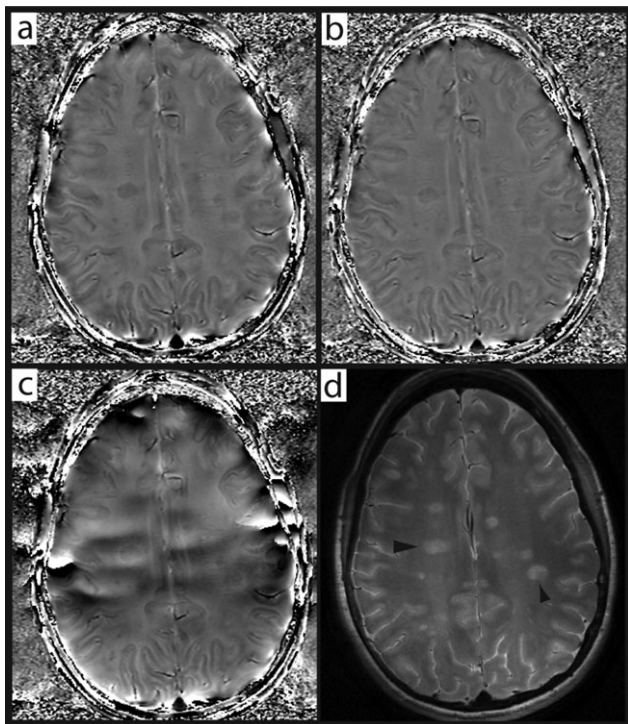


**Figure 6.** Axial images from a 29-year-old RRMS patient acquired at 4.7 T with (a) the new method using  $64f \times 32e$  square fitting and extraction window with 0.0625 filter strength, (b) standard method using 0.125 filter strength, (c) standard method using 0.0625 filter strength, and (d) T2-weighted FSE image identifying inflammatory lesion in MS. Arrowheads in (d) show example lesions used for phase contrast measures.

background removal, which eliminates potential difficulties in unwrapping territories near high susceptibility regions for certain algorithms described by Witoszynskij et al (23) and Zhou et al (29). The moving window background phase estimation could be

implemented with an advanced unwrapping algorithm such as PhiUn; however, areas of rapid phase change or noise could be adversely affected. The gradient fitting method circumvents phase unwrapping by using the spatial gradient of the phase data to determine polynomial coefficients to the raw phase. This local smoothing allows implementation of a weaker standard high pass filter, which dramatically improves tissue contrast and visualization compared to standard filtering. A 0.0625 strength filter was used as the weakest filter in this study because areas with rapidly varying background phase were studied; however, smaller filter strengths could be implemented for even less phase suppression in areas with less significant background fields. As well, the 0.0625 filter closely approximated the ideal phase in simulation and there may be minimal benefit in applying a weaker filter than this. In addition, there is no need for tissue segmentation or masking as with other methods where an accurate brain volume must be delineated (6). The gradient fitting moving window algorithm does not use masking, yet generally performs well at brain edges because the algorithm is designed so the fitting window should contain an adequate number of voxels for polynomial estimation. The final image consists of overlapping extraction windows, originating from a smaller central region within their respective fitting windows. If the fitting window is at the edge of brain tissue with some voxels containing brain and most containing air/skull, there must be a minimum of voxels which extend from the fitting window edge into the extraction window. If brain tissue only represents a few voxels near the edge of the fitting window alone, this will not be included in the extraction window and subsequently the final image. In addition, the edges of the extraction window are weighted less strongly with multiplication of a 2D Hanning window to negate effects of potentially poor background phase removal at brain edges. The method does not require a 3D

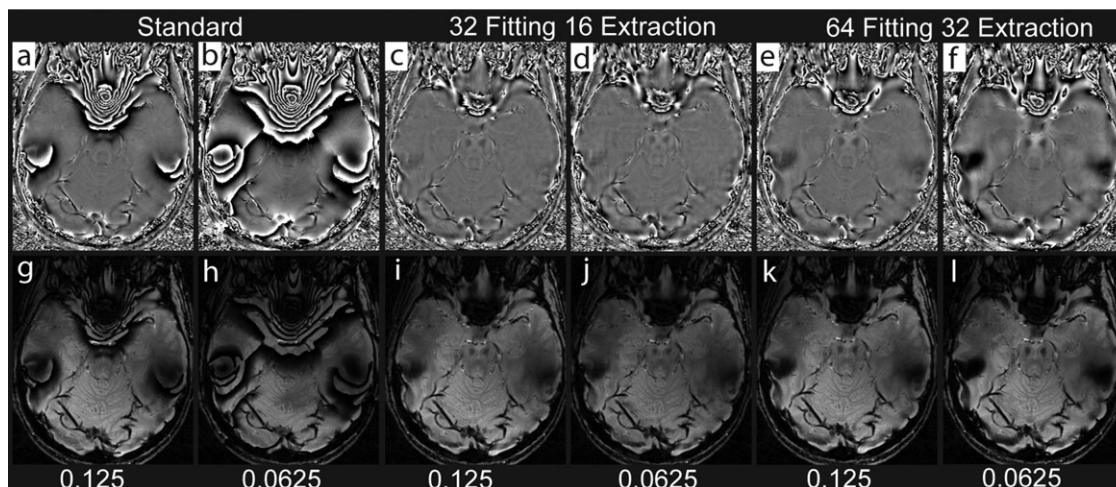


**Figure 7.** 4.7 T images from a 28-year-old volunteer, phase images (top) and SWI images (bottom) showing the midbrain with substantia nigra, left middle cerebral artery, and cerebellum. Standard filtering using (a,g) 0.125 filter strength and (b,h) 0.0625 filter strength. New background phase removal using  $32f \times 16e$  fitting and extraction window with (c,i) 0.125 filter strength and (d,j) 0.0625 filter strength. New background phase removal using  $64f \times 32e$  fitting and extraction window with (e,k) 0.125 filter strength and (f,l) 0.0625 filter strength.

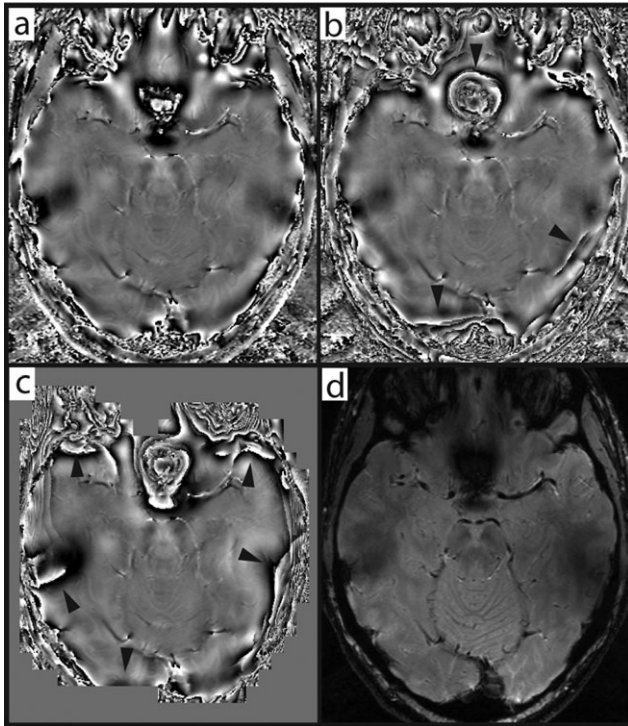


**Figure 8.** 4.7 T images from a 25-year-old volunteer. In each phase image (a–c), the background phase is locally estimated using a moving window third-order polynomial fit. The coefficients for this polynomial are determined using (a) a least-squares fit from the phase gradient data, (b) a direct polynomial fit using an unwrapped phase image with PhiUn, and (c) a direct polynomial fit using an unwrapped phase image with PRELUDE. The magnitude image is shown in (d). Arrowheads in (b,c) identify areas that were not properly unwrapped by PhiUn or PRELUDE but were correctly depicted with the gradient method. The filter width was 0.0625 and the fitting and extraction windows were  $64f \times 32e$  for a–c.

volume but future implementations could utilize a 3D approach. Every iteration must estimate the local phase followed by Hanning filtering, causing total processing time to depend on the extraction window size and the time of these two operations. For one slice of a  $512 \times 512$  matrix using an extraction window of 32, the algorithm took 33.5 seconds but an extraction window of 64 took 6.8 seconds on a computer with a 2.66 GHz core i7 processor.

Quantitative phase analysis with the new method compared to standard phase filtering show higher accuracy in simulation and provides more contrast in vivo using a low filter strength and a fitting window at least as large as the structure of interest. The standard filtering method has drawbacks with either strong or weak filter strengths. If the filter is strong enough to suppress background fields, the phase in the center of structures is suppressed, leading to less contrast and altered phase values (11). Conversely, if the filter strength is weak, the background field may not be removed, confounding visualization of tissue. The new method addresses these conflicting issues apparent in standard filtering and closely approximates the phase profile of large structures while still remov-

ing the background phase in simulation provided an adequately sized fitting window. Although a range of fitting parameters were examined, different fitting window sizes produce similar results in vivo as most brain structures are relatively small compared to the whole image. Furthermore, the extraction window should be smaller than the fitting window for the best results to avoid spurious edge effects using a low-order polynomial fit. The caudate has much more contrast because traditional filtering often does not fully remove phase wraps within this structure which depresses phase values. The putamen has increased contrast with the new method, but it is not significantly different between methods because it contains high spatial frequencies with a strong slope in the phase profile (Fig. 5e).

Improved visualization of brain edges, structures, and lesions was demonstrated in simulation and in vivo. However, artifact is observed when the fitting window was smaller than the structure of interest because the polynomial is being fit to the structures, not primarily the background. This can be avoided with attention to the size of the fitting window assuring that it is larger than 32 for a  $512 \times 512$  image matrix. The lesions examined represent a subset of lesions in MS, as some lesions appear either only in phase or T2-weighted images (26,30). With the new method, enhanced contrast and improved background removal in all brain areas could further delineate phase lesions. Other potential applications include investigating tissue or pathology near the brain edge such as subarachnoid hemorrhage (31), arteriovenous malformations (31), and cortical MS lesions (32). The gradient fit method for determining a polynomial background approximation may have performed better than a direct fit using PRELUDE and PhiUn in areas containing substantial noise because the average phase gradient values over a whole fitting window still accurately estimates the background. If unwrapping fails to remove phase wraps, the background phase cannot be accurately fit using the described methods.

In conclusion, a new background phase removal method has been developed that uses the spatial gradient of the raw phase image to determine the coefficients for a low-order local polynomial fit without prior unwrapping. This allows the use of weaker filter strengths to optimize structure and lesion contrast and enables improved removal of background phase compared to the standard filtering method.

## REFERENCES

1. Duyn JH, van Gelderen P, Li TQ, de Zwart JA, Koretsky AP, Fukunaga M. High-field MRI of brain cortical substructure based on signal phase. *Proc Natl Acad Sci U S A* 2007;104:11796–11801.
2. He X, Yablonskiy DA. Biophysical mechanisms of phase contrast in gradient echo MRI. *Proc Natl Acad Sci U S A* 2009;106:13558–13563.
3. Ogg RJ, Langston JW, Haacke EM, Steen RG, Taylor JS. The correlation between phase shifts in gradient-echo MR images and regional brain iron concentration. *Magn Reson Imaging* 1999;17:1141–1148.

4. Haacke EM, Xu Y, Cheng YC, Reichenbach JR. Susceptibility weighted imaging (SWI). *Magn Reson Med* 2004;52:612–618.
5. Wharton S, Schafer A, Bowtell R. Susceptibility mapping in the human brain using threshold-based k-space division. *Magn Reson Med* 2010;63:1292–1304.
6. Neelavalli J, Cheng YCN, Jiang J, Haacke EM. Removing background phase variations in susceptibility-weighted imaging using a fast, forward-field calculation. *J Magn Reson Imaging* 2009;29:937–948.
7. Hammond KE, Metcalf M, Carvajal L, et al. Quantitative in vivo magnetic resonance imaging of multiple sclerosis at 7 Tesla with sensitivity to iron. *Ann Neurol* 2008;64:707–713.
8. Hopp K, Popescu BF, McCrear RP, et al. Brain iron detected by SWI high pass filtered phase calibrated with synchrotron X-ray fluorescence. *J Magn Reson Imaging* 2010;31:1346–1354.
9. Haacke EM, Ayaz M, Boikov AS, Kido DK, Kirsch WM. Imaging cerebral microbleeds using susceptibility weighted imaging: one step toward detecting vascular dementia. *J Magn Reson Imaging* 2010;31:142–148.
10. Wharton S, Bowtell R. Whole-brain susceptibility mapping at high field: a comparison of multiple- and single-orientation methods. *Neuroimage* 2010;53:515–525.
11. Walsh AJ, Wilman AH. Susceptibility phase imaging with comparison to R2 mapping of iron-rich deep gray matter. *Neuroimage* 2011;57:452–461.
12. Denk C, Rauscher A. Susceptibility weighted imaging with multiple echoes. *J Magn Reson Imaging* 2010;31:185–191.
13. McPhee KC, Denk C, Al Rekabi Z, Rauscher A. Bilateral filtering of magnetic resonance phase images. *Magn Reson Imaging* 2011;29:1023–1029.
14. Ng A, Johnston L, Chen Z, Cho ZH, Zhang J, Egan G. Spatially dependent filtering for removing phase distortions at the cortical surface. *Magn Reson Med* 2011;66:784–793.
15. Tong KA, Ashwal S, Obenaus A, Nickerson JP, Kido D, Haacke EM. Susceptibility-weighted MR imaging: a review of clinical applications in children. *AJNR Am J Neuroradiol* 2008;29:9–17.
16. Schweser F, Deistung A, Lehr BW, Reichenbach JR. Quantitative imaging of intrinsic magnetic tissue properties using MRI signal phase: an approach to in vivo brain iron metabolism? *Neuroimage* 2011;54:2789–2807.
17. Liu T, Khalidov I, de Rochefort L, et al. A novel background field removal method for MRI using projection onto dipole fields (PDF). *NMR Biomed* 2011;24:1129–1136.
18. Yao B, Li TQ, Gelderen P, Shmueli K, de Zwart JA, Duyn JH. Susceptibility contrast in high field MRI of human brain as a function of tissue iron content. *Neuroimage* 2009;44:1259–1266.
19. Meyers S, Eissa A, Wilman AH. Advantages of a local polynomial filter with moving window for phase reconstruction in susceptibility-weighted imaging. In: *Proc 18th Annual Meeting ISMRM, Stockholm; 2010* (abstract 4991).
20. Bagher-Ebadian H, Jiang Q, Ewing JR. A modified Fourier-based phase unwrapping algorithm with an application to MRI venography. *J Magn Reson Imaging* 2008;27:649–652.
21. Rauscher A, Barth M, Reichenbach JR, Stollberger R, Moser E. Automated unwrapping of MR phase images applied to BOLD MR-venography at 3 Tesla. *J Magn Reson Imaging* 2003;18:175–180.
22. Langley J, Zhao Q. Unwrapping magnetic resonance phase maps with Chebyshev polynomials. *Magn Reson Imaging* 2009;27:1293–1301.
23. Witoszynskij S, Rauscher A, Reichenbach JR, Barth M. Phase unwrapping of MR images using Phi UN—a fast and robust region growing algorithm. *Med Image Anal* 2009;13:257–268.
24. Wang Y, Yu Y, Li D, et al. Artery and vein separation using susceptibility-dependent phase in contrast-enhanced MRA. *J Magn Reson Imaging* 2000;12:661–670.
25. Haacke EM, Ayaz M, Khan A, et al. Establishing a baseline phase behavior in magnetic resonance imaging to determine normal vs. abnormal iron content in the brain. *J Magn Reson Imaging* 2007;26:256–264.
26. Haacke EM, Makki M, Ge YL, et al. Characterizing iron deposition in multiple sclerosis lesions using susceptibility weighted imaging. *J Magn Reson Imaging* 2009;29:537–544.
27. Sedlacik J, Kutschbach C, Rauscher A, Deistung A, Reichenbach JR. Investigation of the influence of carbon dioxide concentrations on cerebral physiology by susceptibility-weighted magnetic resonance imaging (SWI). *Neuroimage* 2008;43:36–43.
28. Jenkinson M. Fast, automated, N-dimensional phase-unwrapping algorithm. *Magn Reson Med* 2003;49:193–197.
29. Zhou K, Zaitsev M, Bao S. Reliable two-dimensional phase unwrapping method using region growing and local linear estimation. *Magn Reson Med* 2009;62:1085–1090.
30. Eissa A, Lebel RM, Korzan JR, et al. Detecting lesions in multiple sclerosis at 4.7 Tesla using phase susceptibility-weighting and T2-weighting. *J Magn Reson Imaging* 2009;30:737–742.
31. Kudo K, Fujima N, Terae S, et al. Spinal arteriovenous malformation: evaluation of change in venous oxygenation with susceptibility-weighted MR imaging after treatment. *Radiology* 2010;254:891–899.
32. Calabrese M, Filippi M, Rovaris M, et al. Morphology and evolution of cortical lesions in multiple sclerosis. A longitudinal MRI study. *Neuroimage* 2008;42:1324–1328.